THE JOURNAL OF PHYSICAL CHEMISTRY C
A JOURNAL OF THE AMERICAN CHEMICAL SOCIETY

pubs.acs.org/JPCC

Article

Direct Imaging of the Structural and Morphological Evolution of Epitaxial $LiCoO_2$ Films during Charge and Overcharge

Published as part of The Journal of Physical Chemistry virtual special issue "Esther Sans Takeuchi Festschrift".

Widitha Samarakoon, Jiangtao Hu, Miao Song, Mark Bowden, Nabajit Lahiri, Jia Liu, Le Wang, Timothy Droubay, Krishna Koirala, Hua Zhou, Zhenxing Feng, Jinhui Tao,* and Yingge Du*

Cite This: *J. Phys. Chem. C* 2022, 126, 15882–15890

Read Online

ACCESS | Metrics & More | Article Recommendations | Supporting Information

ABSTRACT: The capacity decay of layered cathodes in high-voltage applications underscores the need to utilize accurate and precise techniques to understand the underlying mechanisms. Here, we use well-defined epitaxial $LiCoO_2$ (LCO) films on $SrRuO_3/SrTiO_3$ (SRO/STO) with controlled orientations and defect structures along with *in situ* electrochemical atomic force microscopy to probe the structural and morphological evolutions during the charge and overcharge processes. We quantitatively show the morphological changes in both the reversible delithiation regime and the irreversible over-delithiation regime and correlate the overall electrochemical behaviors to atomic scale defect evolutions in the films. We also observe a significantly lower charging capacity for LCO/SRO/STO(111) compared to that of LCO/SRO/STO(001) films of the same thickness, which is ascribed to different types of atomic scale defects formed during the film growth process. Our high-resolution scanning transmission electron microscopy (STEM) and electron energy loss spectroscopy (EELS) studies reveal that the antiphase boundaries in LCO/SRO/STO(111) act as viable channels for Li migration but are more susceptible to irreversible phase transitions, which then block subsequent Li diffusion. The failure mechanisms developed here may provide insight into the design of future cathode materials.

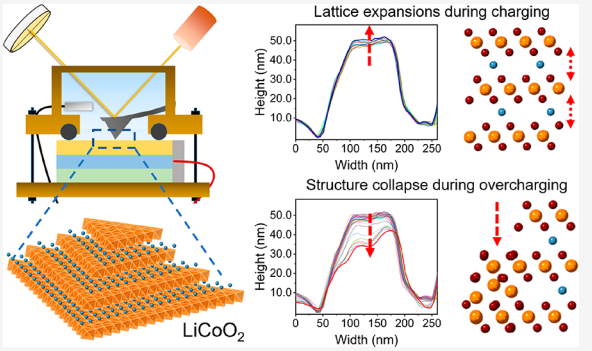

INTRODUCTION

Layered $LiCoO_2$ (LCO) has been studied extensively as a cathode material in lithium-ion batteries (LIBs) because of its excellent reversibility and high theoretical capacity.[1−3] However, in realistic applications, only ∼140 mAh g^{-1} discharge capacity is realized corresponding to a cutoff voltage of ∼4.2 V,[2,4] which is not sufficient to meet the growing demand for high energy density LIBs, particularly for use in electric vehicles (EVs). Although charging LCO to a high voltage is a possible method to boost the energy density by extracting more Li ions from the structure,[5−9] over-delithiation leads to serious capacity attenuation during cycling. This can be attributed to two aspects: the detrimental interfacial side reactions resulting from irreversible phase transformations and nonuniform stresses induced by the inhomogeneous Li distribution during lithiation/delithiation in LCO, which ultimately leads to structural damage and diffusion blockage.[10−12] Different LCO failure mechanisms, such as interfacial redox reactions[13,14] and oxygen release,[15,16] have been proposed to study high-voltage applications. However, limited attention has been paid on correlating basic but important attributes such as surface roughness, crystal facet orientation, and defects distribution in LCO to electrochemical degradations at a fundamental level by using quantitative analysis.

Epitaxial LCO thin films with controlled orientation, atomically sharp interfaces, and tunable defects have been used as model systems to study their intrinsic electrochemical behaviors. The absence of additives such as carbon black and polymeric binders normally used in powder-based cathodes makes it easier and cleaner to perform structural and chemical characterizations.[17−23] Pulsed laser deposition (PLD) is the most widely used technique to synthesize epitaxial LCO films while one of the widely used substrates is single-crystalline $SrTiO_3$ (STO). For instance, LCO can grow epitaxially on STO(001) and STO(111) with LCO(104) and LCO(001) facets parallel to the substrate surface, respectively.[4,20] A buffer layer of metallic $SrRuO_3$ (SRO) has been grown prior to the LCO deposition to act as the current collector.[22,23] It was

Received: March 21, 2022
Revised: June 14, 2022
Published: September 12, 2022

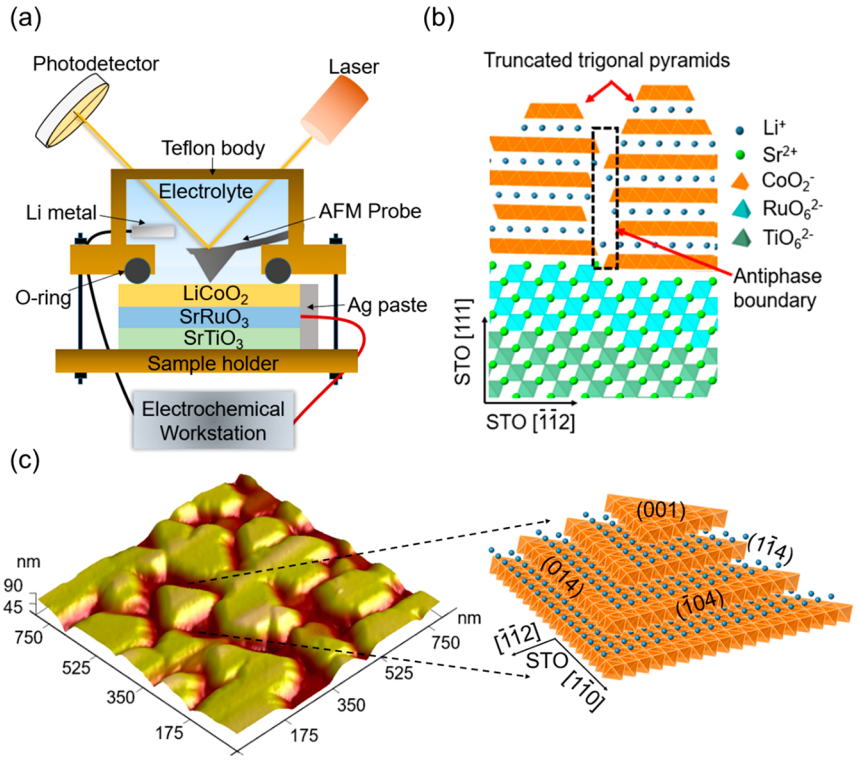

Figure 1. (a) Scheme of the experimental setup for *in situ* AFM monitoring. A buffer layer of SRO is used as the electrical contact to maximize the current collection. (b) Crystal structure model of the LCO/SRO/STO(111) sample cut along the STO/SRO(110) plane. LCO grows epitaxially on SRO/STO (111) so that Li-containing planes are parallel to the surface. The step terrace at the (111)-cleaved STO surface gives rise to antiphase boundary defects in LCO which act as channels for Li^+ to diffuse from the bulk of the film to the surface. (c) Surface topography of LCO/SRO/STO(111) imaged by AFM. The surface mostly consists of trigonal-pyramidal islands terminated with (001) planes on the top and {104} family facets on the sides.

shown by using transmission electron microcopy (TEM) that when LCO is charged to voltages over 4.2 V, the irreversible phase transformations from layered LCO to spinel Co_3O_4 or rock-salt CoO occur, primarily on the surface and then propagate into the bulk which contribute to capacity decay.[21,24] Furthermore, *in situ* synchrotron X-ray reflectivity[4] and electrochemical impedance spectroscopy[22] studies revealed that the formation of an unstable and porous cathode–electrolyte interface film on intercalation active {104} facets of epitaxial LCO films causes severe surface degradations during extended cycling. A recent *in situ* TEM study reported that phase transformations on the surface under excessive delithiation conditions contribute towards surface crack formation, thereby aggravating surface corrosion processes in LCO.[19] Despite all these efforts, the mechanistic understanding of the failure of LCO, especially under high-voltage applications, remains ambiguous because of the lack of *in situ* monitoring and quantification of structural and morphological changes at the surface and in the bulk. *In situ* electrochemical atomic force microscopy (EC-AFM) with subnanometer-scaled spatial resolution is a promising technique that has been used along with other high-resolution structural characterization techniques such as TEM to connect the real-time surface topographical evolution with atomic structural evolution to establish a deeper mechanistic understanding.[10,25,26]

In this work, we use epitaxial thin films of LCO as model systems to reveal the atomic to mesoscale structural evolution during charging and overcharging. The onset of delithiation as a result of charging and material failure during overcharging are investigated by virtue of *in situ* EC-AFM along with STEM, X-ray diffraction (XRD), and X-ray photoelectron spectroscopy (XPS). We directly associate the change in surface topography to the delithiation processes occurring in a single (over)charge cycle. The LCO islands in LCO/SRO/STO(111) show a gradual increase in height which is attributed to the Coulombic lattice expansions during reversible Li^+ deintercalation up to ~4.2 V vs Li/Li^+. During over-delithiation, LCO islands on STO(111) show a decrease in island height which is ascribed to the irreversible phase transformation to Co_3O_4 and CoO. These phase transitions significantly disturb the surface topography and block subsequent diffusion of Li^+ from the bulk to the surface via antiphase boundary (APB) defect channels, thereby degrading overall charge transfer. In comparison, LCO/SRO/STO(001) shows a relatively higher degree of delithiation because of the presence of open channels for Li^+ diffusion on the surface. We demonstrate that the orientation-dependent quantitative study enables a deeper mechanistic understanding of the failure modes of LCO during overcharge.

METHODS

LCO thin film samples with ~100 nm thickness were deposited on STO(111) and STO(001) substrates (MTI Corp.) by using PLD. An ~15 nm thick epitaxial buffer layer of SRO was deposited as the electrical contact prior to LCO growth. The SRO layer was deposited at a substrate temperature of 650 °C with an oxygen pressure of 50 mTorr. The LCO layer was deposited at a substrate temperature of 600 °C with an oxygen pressure of 10

https://doi.org/10.1021/acs.jpcc.2c01940
J. Phys. Chem. C 2022, 126, 15882−15890

mTorr. For both layers, laser ablation was performed at a repetition rate of 5 Hz and an energy density of 2 J cm^{-2} with a 248 nm KrF excimer laser source. The details of the system are described elsewhere.[38] After growth, the samples were cooled to room temperature at 25 °C/min under the growth pressure.

The crystal structures of the samples were examined by conducting out-of-plane XRD scans and in-plane ϕ scans using a high-resolution X-ray diffractometer (Rigaku SmartLab). 3D reciprocal space maps (3D RSMs) for the pristine samples were obtained at beamline 33-IDD at Advanced Photon Source, Argonne National Laboratory, with an incident photon energy of 15.5 keV. Cross-sectional TEM samples were prepared by using an FEI Helios NanoLab dual-beam focused ion beam (FIB) microscope and standard lift out procedure along the [110] zone axis of STO(111) substrate. High angle annular dark field STEM (HAADF-STEM) images were collected on a probe-corrected JEOL ARM-200CF microscope operating at 200 kV, with a convergence semiangle of 27.5 mrad and a collection angle range of 68−280 mrad. Co valences in the over-delithiated LCO/SRO/STO(111) sample were determined by Co $L_{2,3}$-edge electron energy loss spectroscopy (EELS) using 0.25 V ch^{-1} dispersion and 0.01 s dwell time.

XPS measurements were performed to probe the surface chemistry on a Kratos AXIS Ultra DLD spectrometer using an Al Kα X-ray source ($h\nu$ = 1486.7 eV, 150 W) operating at a pressure lower than 2×10^{-9} Torr. The thin film samples were mounted on a double-sided Scotch brand tape. High-resolution analysis was performed on an area of 700 × 300 μm^2 at a normal emission angle by using a pass energy of 40 eV and a step size of 0.1 eV. For reference, Au $4f_{7/2}$ of a sputter-cleaned gold foil produces a full width at half-maximum of 0.85 eV at a pass energy of 40 eV. A low-energy electron flood gun was used to neutralize any surface charging, and the data were charge referenced to C 1s (C−C/C−H component) at 285 eV. The XPS data were processed by using CASA software.

Special care was given during sample handling and *ex situ* TEM, XPS, and XRD characterizations for the overcharged LCO samples to minimize the exposure of samples to air as high-valent metal oxides such as overcharged LCO experience chemical instability upon exposure to atmospheric moisture.[27] After *in situ* AFM experiments, the samples were washed with dimethyl carbonate in an argon-filled glovebox and sealed in a Pyrex ampule. Subsequently, XPS and TEM sample mounting were performed in an airtight Ar-filled environments. The time taken to transfer the sample to the instruments was reasonably short which further ensured that exposure to air was kept as low as reasonably achievable.

Before *in situ* experiments were conducted, each thin film sample was individually mounted onto a magnetic AFM sample holder by using epoxy. To make the electrical contact, one corner of the 10 mm × 10 mm sample was scratched with a diamond knife to expose the SRO buffer layer. Then Ag paste was used to make the electrical connection to the exposed SRO buffer layer by using a flattened Ni wire. A Teflon O-ring with a diameter of 6.5 mm was used to seal the electrolyte inside liquid cell. The Ni wire was isolated from the electrolyte since the sample size was larger than the O-ring. The electrochemical cell was assembled with the O-ring and a sealing cap with a thin Li wire as the counter/reference electrode as shown in Figure 1a. Another free sealing cap was used to seal the solution inside after injection, and the setup was ready for *in situ* AFM monitoring.

All *in situ* AFM images were collected in peak force tapping mode at room temperature (23 °C) with a Nanoscope 8 atomic force microscope (J scanner, Bruker) that has been described previously.[28,29] The AFM probe consisted of silicon tips on silicon cantilevers (HA_C Series of ETALON probes, k = 0.26 N/m, tip radius <10 nm; K-TEK Nanotechnology). The electrolyte used was 1.0 M $LiPF_6$ in ethylene carbonate (EC)/ethyl methyl carbonate (EMC) (3:7 weight ratio). The working electrode (mentioned above) was connected to the Solartron 1287 electrochemical workstation by using the Ni wire. A thin Li wire (counter/reference electrode) with a sealing cap was inserted into the electrolyte by using another channel in the electrochemical cell (Figure 1a). A charging voltage was applied from OCV (~3.7 V) to 4.9 V with a uniform scan rate of 0.3 mV/s. Under typical imaging conditions, a scan rate of 1 Hz was used to collect images.

To minimize the effect of raster scanning cantilever on the intrinsic morphological evolution, several protocols were followed. First, the imaging force was minimized to working value (~50 pN) that still allowed the tip to track the surface while avoiding any measurable effect on the surface topography due to scanning. This was verified by zooming out to a larger scan area and comparing the surface to the smaller scan area. Images were also collected at different scan angles to make sure trace and retrace profiles were always overlapped to eliminate the possibility of imaging artifacts due to tip contamination. The images were analyzed by using the image processing software packages NanoScope Analysis 2.0 (Bruker) and Scanning Probe Image Processor 5.1.4 (Image Metrology A/S).

Cyclic voltammetry (CV) was performed on a control LCO/SRO/STO(111) sample before conducting *in situ* studies to verify the effectiveness of SRO buffer layer as a current collector. CV was conducted by using a three-electrode setup with a Li wire as the counter and reference electrodes and the LCO film as the working electrode. To prepare the working electrode, one corner of the LCO film was scratched by using a diamond tool to expose the SRO buffer layer. Then a Cu wire was attached to the SRO layer by using high-purity Ag paste. The wire contact and the back and sides of the LCO film were covered with inert epoxy (Locite 9460) so that only the film surface was exposed. The epoxy was allowed to fully cure for 48 h. The CV was conducted from an OCV of 2.7 to 4.9 V with a scan rate of 0.5 mV/s by using 1.0 M $LiPF_6$ in EC/EMC (3:7 weight ratio) as the electrolyte.

RESULTS AND DISCUSSION

Figure 1a shows a scheme of the *in situ* EC-AFM cell used to probe the mesoscale topography evolution during delithiation in LCO/SRO/STO samples. This setup allows us to track nanoscale structural changes in cathode materials during electrochemical processes. For the LCO/SRO/STO(111) sample, Li-containing planes are oriented parallel to the substrate surface as shown in Figure 1b.[20,22] The epitaxial relationship has been further confirmed by our high-resolution out-of-plane XRD scans (Figure S1a), which show peaks corresponding to (00l) planes of LCO and (111) and (222) planes of STO. Peaks for SRO are also visible showing the cube-on-cube arrangement of SRO with STO.[22,23] This is further verified by the 3D RSM about the STO(113) peak which shows that the SRO layer is fully strained to the STO substrate, and the LCO layer is partially relaxed (Figure S1b). Moreover, the step terrace at the STO(111) surface gives rise

https://doi.org/10.1021/acs.jpcc.2c01940
J. Phys. Chem. C 2022, 126, 15882−15890

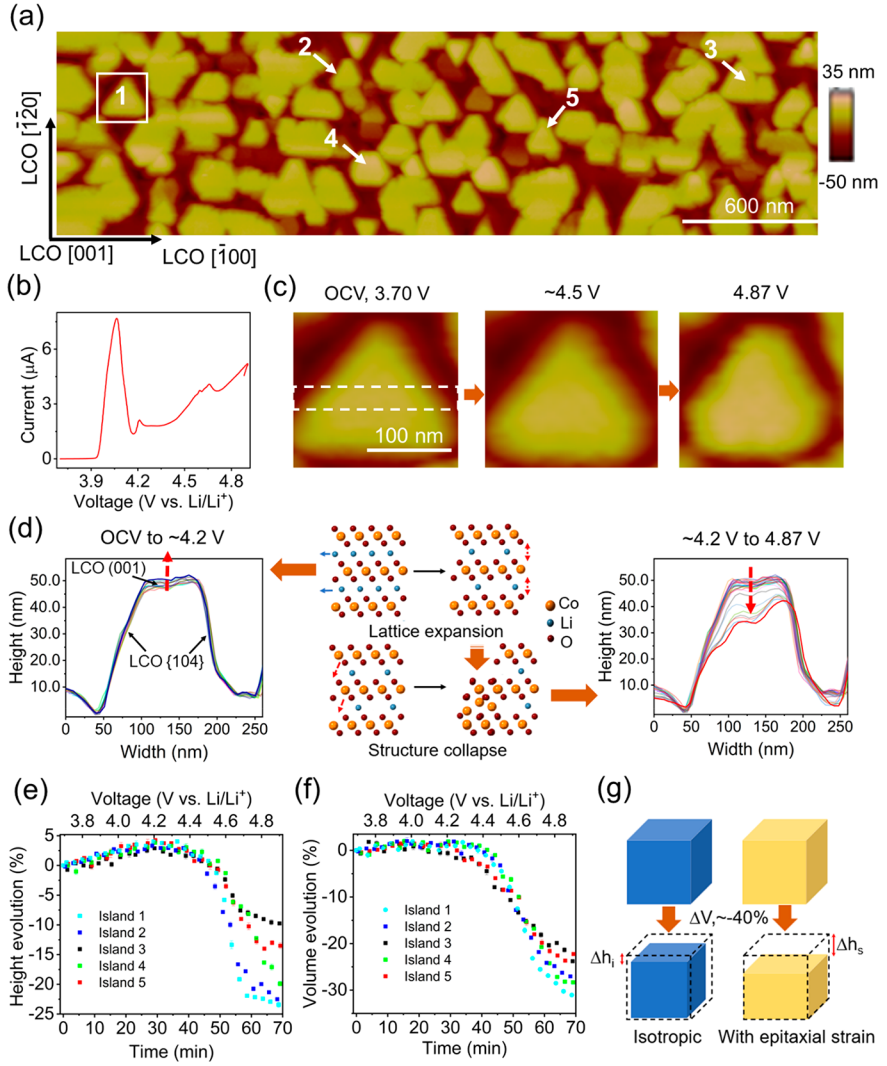

Figure 2. *In situ* AFM monitoring of the LCO/SRO/STO(111) sample. (a) AFM image of the surface at open circuit voltage (OCV). Islands used for subsequent height and volume measurements are labeled. (b) Cyclic voltammetry (CV) curves for LCO/SRO/STO(111) sample. (c) Shape evolution of island 1 from an OCV of 3.7 to ~4.9 V. (d) Evolution of island 1 cut along a horizontal plane from OCV to ~4.2 V (left) and from ~4.2 to ~4.9 V (right). The crystal model (middle) further illustrates the structural evolution. The arrows in the crystal model illustrate reversible deintercalation of Li^+ (blue) and lattice expansion/contraction (red). The percentage change in height (e) and volume (f) of islands 1−5. (g) Scheme showing the expected height decrease for volume shrinkage (ΔV) of ~40% which occurs during the phase transformation from LCO to Co_3O_4 and ultimately CoO. Δh_i and Δh_s denote height drops for isotropic and epitaxially strained processes, respectively, where Δh_i is ~−16% and $-40\% < \Delta h_s < -16\%$ (Table S1).

to multiple single crystalline (001)-oriented LCO domains separated by APBs that are proposed to act as alternative diffusion channels for Li^+ (Figure 1b).[30] The surface morphology of a typical pristine LCO/SRO/STO(111) sample is revealed by AFM (Figure 1c). The surface consists of isolated, truncated trigonal-pyramidal islands. In agreement with previous studies, the island surfaces are (001) oriented, and the sides exhibit {104} facets,[20−22] most likely because (001) and {104} planes have the lowest surface energy in LCO.[31]

Figure 2a shows an AFM image of a pristine LCO/SRO/STO(111) sample before applying any voltage. The LCO surface is largely covered by isolated trigonal-pyramidal islands out of which a minor fraction is rotated by 180°. With the help of X-ray stereographic analysis and indexing lattice direction along STO[1$\bar{1}$0] (also equivalent to LCO [$\bar{1}$00]) during the TEM liftout procedure, we assign facets for the 180° rotated and unrotated islands as shown in Figure S2a. We also conducted X-ray ϕ scans to further explore the crystal structure and orientation of in-plane domains in the film. As shown in Figure S2b, STO shows a 6-fold symmetry which is characteristic of the *p*-6*mm* symmetry of the STO(111) surface. LCO shows two domains rotated by 180°, each consisting of 3-fold 3-*mm* type symmetry which agrees with previous scanning electron microscopy (SEM) studies.[17] The markedly different intensities in the X-ray ϕ scan for the two LCO domains show that majority of the film consists of one type of domain which is ascribed to the predominant TiO_2 termination of the STO substrate.[20]

In comparison, the XRD pattern for the LCO/SRO/STO(001) sample shows peaks for the (00l) planes of SRO/STO and the (104) peak of LCO (Figure S3a) confirming the cube-on-cube epitaxial growth that has been observed previously.[18−20] The SRO buffer layer is strained to the STO substrate, and the LCO layer is fully relaxed (Figure S3b). The Li-containing planes in LCO are oriented ~55° to the

https://doi.org/10.1021/acs.jpcc.2c01940
J. Phys. Chem. C 2022, 126, 15882−15890

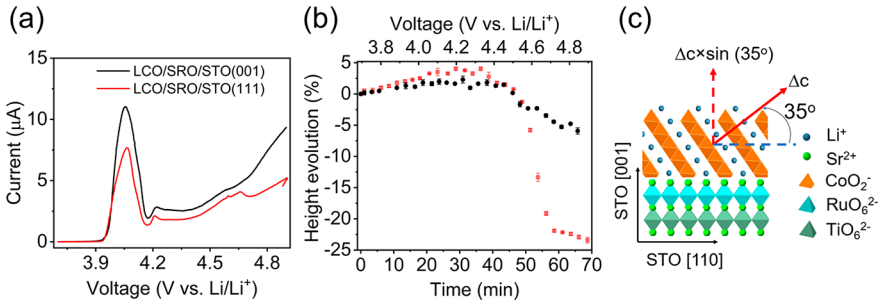

Figure 3. *In situ* AFM monitoring of the LCO/SRO/STO(001) sample. (a) Comparison of CV for LCO/SRO/STO(111) and LCO/SRO/STO(001) samples. (b) Height evolution of an individual grain (grain 2 in Figure S4) for the LCO/SRO/STO(001) sample (black). For comparison, the height change of a representative island in LCO/SRO/STO(111) is also included (red). (c) A lattice model showing the *c*-axis orientation of LCO in the LCO/SRO/STO(001) sample.

substrate surface, and the exposed (104) planes have open channels for Li^+ out-diffusion.[21,22] In contrast to the surface morphology consisting largely of isolated islands in LCO/SRO/STO(111), a relatively dense surface consisting of grains/grain boundaries is observed in LCO/SRO/STO(001) (Figure S4). These grains are oriented along the STO ⟨110⟩ direction and terminated by the (104) plane on the top as dictated by the epitaxial relationship between LCO and SRO/STO(001).[20]

Prior to conducting *in situ* EC-AFM experiments, CV was performed on an LCO/SRO/STO(111) sample with an ∼100 nm LCO layer. As shown in Figure S5, the CV shows all the expected anodic and cathodic peaks for LCO in the voltage range.[21] This suggests that the SRO buffer layer helps to capture the intrinsic electrochemical behavior of LCO. Subsequently, *in situ* EC-AFM measurements were performed on the LCO/SRO/STO sample. An extreme cutoff voltage of 4.9 V vs Li/Li^+ was chosen so that complete structural evolution from the onset of delithiation to material failure can be captured by AFM. A CV curve of the LCO/SRO/STO(111) sample (Figure 2b) clearly shows a large peak at ∼4.0 V as a result of the first-order transition between two hexagonal phases with *c*-axis lattice parameters of 14.08 and 14.2 Å, respectively.[32] A monotonic increase in the current beyond 4.5 V is observed, which corresponds to electrolyte oxidation/decomposition.[33] The surface morphology evolution of LCO/SRO/STO(111) during the anodic half cycle (Video S1) shows that the truncated pyramidal islands maintain a regular triangular base for voltages less than ∼4.5 V. Beyond that, the edges of the pyramidal islands get less sharp and become narrower as shown in Figure 2c. This is likely caused by the breakdown of the cathode−electrolyte interface layers on the intercalation-active {104} facets in the pyramidal islands and subsequent corrosion of LCO by HF, which is a product of electrolyte decomposition.[34,19]

To gain more insight into the structural evolution of LCO from the onset of delithiation to material failure, we focused on randomly selected pyramidal islands on the LCO/SRO/STO(111) sample. The step profile evolution (as indicated in Figure 2c) of island 1 shows a gradual expansion along the *c*-axis of LCO up to a voltage of ∼4.2 V vs Li/Li^+ followed by a continuous drop in island height (Video S2) from ∼4.2 to ∼4.9 V. This observation is summarized in Figure 2d as well. To corroborate these insights with quantitative evidence, we monitored the height and volume changes of five representative islands labeled in Figure 2a. As shown in Figure 2e, we observed a gradual increase in the height of all islands up to a voltage of ∼4.2 V, corresponding to an average increase of ∼3% in the *c*-axis of LCO. This increase in the *c*-axis is a result of Coulombic lattice expansions during reversible deintercalation and is consistent with previous *in situ* XRD experiments.[32,35,36]

To understand the reason for the subsequent decrease in island height, we investigated phase transitions occurring in LCO during delithiation. LCO undergoes a phase transformation from the layered $R\bar{3}m$ structure to a spinel structure consisting of both Li and Co atoms at tetrahedral sites when more than 50% of Li^+ is released locally.[21] It has been reported that this spinel structure reverts back to the initial layered phase upon lithiation if the charging cutoff is ∼4.2 V vs Li/Li^+.[21] However, during a high-voltage delithiation (overcharging) process, Li ions are further removed from LCO, leading to an irreversible phase transition to a Co_3O_4 spinel structure in which tetrahedral and octahedral sites are occupied by Co^{2+} and Co^{3+} ions, respectively.[19,21,37] This spinel Co_3O_4 phase can further reduce by losing oxygen to form the rock-salt CoO phase under extreme delithiation conditions.[24,37] The formation of both these phases is also associated with a significant volume reduction[19] which is estimated to be as large as ∼40% (Table S1). The measured volume changes shown in Figure 2f provide direct quantitative evidence of this volume reduction (∼30%), indicating that nearly all the surface LCO islands are transformed to Co_3O_4 or CoO. Furthermore, beyond 4.2 V, the average decrease in island height is ∼20%, which is greater than the expected drop in height (∼16%) for an isotropic volume shrinkage (Table S1). This difference is a consequence of the epitaxial strain provided by the substrate (Figure S1b) which restricts the in-plane movement of LCO as illustrated in Figure 2g.

For comparison, we also investigated the surface morphology evolution of the LCO/SRO/STO(001) sample during the anodic half-cycle (Video S3). Figure 3a shows the comparison of CVs for the two samples LCO/SRO/STO(111) and LCO/SRO/STO(001). The amount of LCO activated during the CV is the same for both samples since they have the same nominal thickness (∼100 nm) and surface area (∼0.33 cm^2) which is defined by the area enclosed by the O-ring (∼0.65 cm inner diameter). We also compared the height evolution of an individual grain in LCO/SRO/STO (001) (grain 2 in Figure S4) to a representative island (island 1) in LCO/SRO/STO(111) (Figure 3b). The measured height increase upon charging (for a voltage up to ∼4.2 V vs Li/Li^+) and the height decrease upon overcharging for LCO/SRO/STO (001) are considerably smaller compared to those observed in LCO/

https://doi.org/10.1021/acs.jpcc.2c01940
J. Phys. Chem. C 2022, 126, 15882−15890

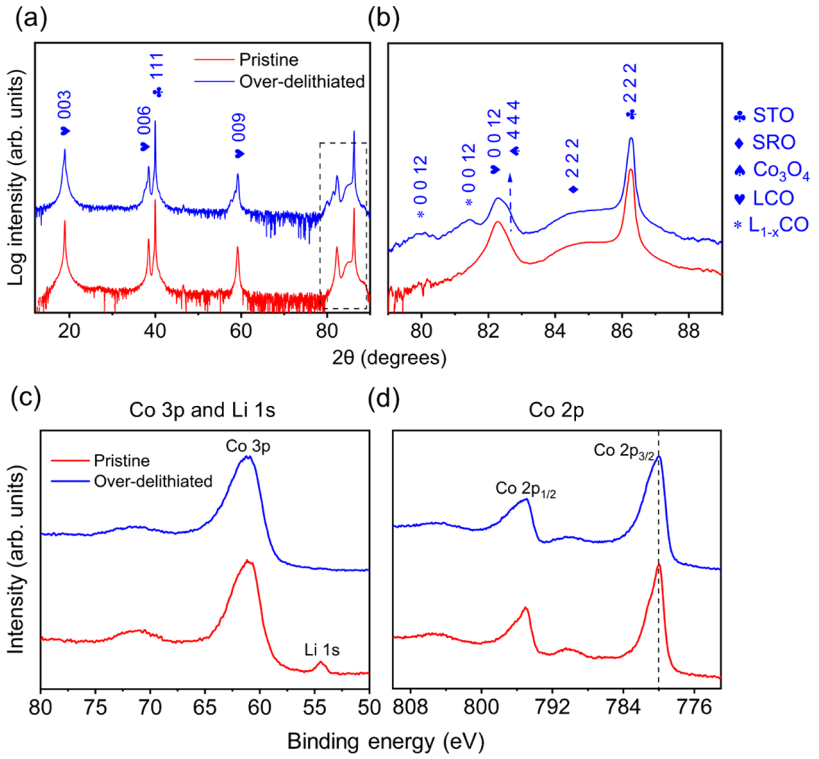

Figure 4. XRD and XPS characterization of the LCO/SRO/STO(111) sample. (a) Comparison of high-resolution out-of-plane XRD θ–2θ scans for the over-delithiated and pristine samples with a zoomed-in region about the STO (222) Bragg peak shown in (b). (c) Comparison of Co 3p and Li 1s XPS and (d) Co 2p XPS for over-delithiated and pristine samples.

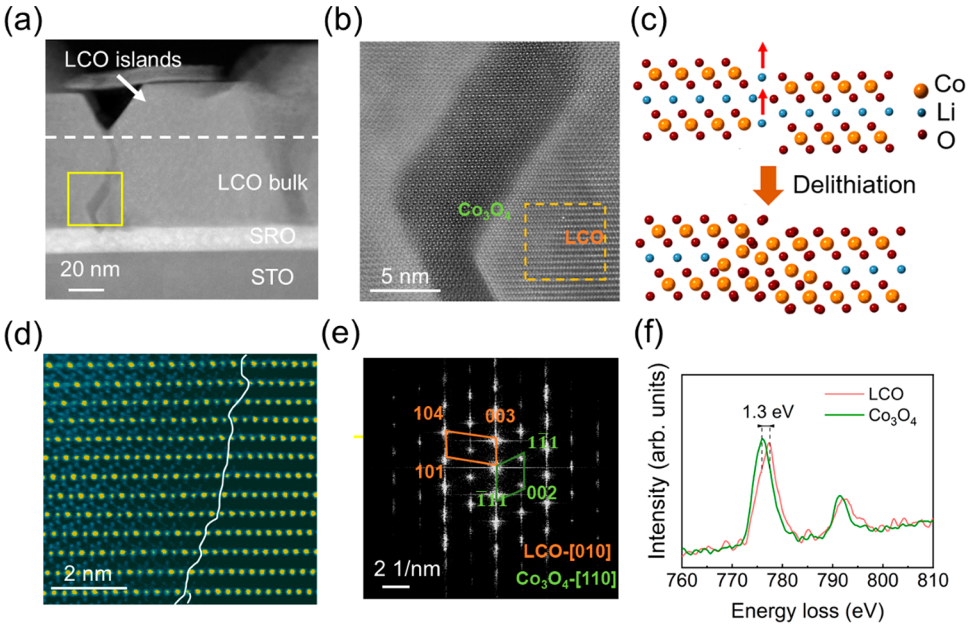

Figure 5. HAADF-STEM characterization of the over-delithiated LCO/SRO/STO(111) sample. (a) Low-magnification image showing the epitaxial heterostructure viewed along the STO[110] zone axis. The dashed line indicates the boundary between LCO film bulk and surface islands. (b) High-resolution image of the region enclosed by the solid yellow box in (a). The entire antiphase boundary (APB) and regions nearby have been transformed to the Co_3O_4 phase. (c) Crystal model showing the layered LCO to Co_3O_4 phase transition occurring at the APB due to localized delithiation. (d) High-magnification HAADF-STEM image of the yellow dashed box region in (b). The white line marks the nominal separation between the LCO and Co_3O_4 regions. (e) Fast Fourier transform of (d). (f) Core-loss EELS on the Co-$L_{2,3}$ edge showing an energy shift to lower energy in the Co_3O_4 region.

SRO/STO(111). It should be noted that the *c*-axis of LCO in LCO/SRO/STO(001) is no longer oriented along the vertical direction. Therefore, only a component of the *c*-axis expansion, given by $\Delta c \times \sin(35°)$ (Figure 3c), is probed by AFM. Thus, we show quantitatively that the morphology changes measured by AFM is heavily affected by the crystallographic orientation.

https://doi.org/10.1021/acs.jpcc.2c01940
J. Phys. Chem. C 2022, 126, 15882−15890

To corroborate the findings from *in situ* EC-AFM, we further examined the crystal structure and surface chemistry of LCO films using XRD and XPS, respectively. Figure 4a shows the comparison of XRD patterns for pristine and over-delithiated LCO/SRO/STO(111) samples. A zoomed-in plot about the STO(222) Bragg peak is presented in Figure 4b. The (00l) peaks for pristine LCO are still visible with a comparable intensity confirming that the film still consists of a significant fraction of pristine layered LCO most likely in bulk regions. Furthermore, two other peaks appear at low angles, namely 81.41° and 79.9°, which correspond to ∼0.9 and 2.4% expansions along the *c*-axis as a result of partial delithiation ($Li_{1-x}CoO_2$). This indicates the presence of regions with different degrees of delithiation. By comparison of electrochemical properties previously obtained by using the potentiostatic intermittent titration technique (PITT) for PLD grown epitaxial LCO films, the observed levels of lattice expansions correspond to ∼10% ($Li_{0.9}CoO_2$) and 50% ($Li_{0.5}CoO_2$) of Li^+ extraction, respectively.[32] Moreover, we noticed the appearance of a shoulder to the right of the LCO(00 12) peak at an angle of ∼82.8°, which corresponds to the (444) peak of Co_3O_4 phase (Figure 4b). The similarities between the crystal structures of LCO and Co_3O_4 make a topotactic phase transition between them possible.[17,21] The relatively low intensity in the Co_3O_4 peak suggests that it constitutes a small fraction of the film.[21]

Figures 4c and 4d show the core-level XPS Co 3p and Co 2p spectra for the pristine and over-delithiated LCO/SRO/STO(111) samples, respectively. As seen in Figure 4c, the Li 1s signal is no longer detectable in the over-delithiated sample, indicating that a complete delithiation occurred at the surface region, which is expected because of the high cutoff voltage used. The Co 2p spectrum for the over-delithiated sample shows a measurable wider full width at half-maximum (FWHM) (2.5 eV vs 1.8 eV for the pristine sample), most likely due to the mixed contributions from both Co^{2+} and Co^{3+}.[39] XRD and XPS results suggest that a phase change from LCO to Co_3O_4 or CoO occurs predominantly in the surface region of LCO/SRO/STO(111) after over-delithiation, but mixed phases with Li_xCoO_2 are expected in the bulk film.

To further assess the structural and interfacial degradation during the delithiation process, cross-sectional HAADF-STEM imaging was performed as shown in Figures 5 and S6. Figure 5a shows a low-magnification TEM image of the over-delithiated LCO/SRO/STO(111) sample viewed along the STO[110] zone axis. The LCO film can be divided into two regions: LCO bulk close to the LCO/SRO interface and isolated islands on the surface. Further inspection of the over-delithiated LCO/SRO/STO(111) sample reveals a gradual transition from the layered LCO to spinel Co_3O_4 and ultimately rock-salt CoO when moving from the bulk film to the surface (Figure S6). This observation is consistent with the highly localized delithiation expected from the {104}-faceted surface islands and the continuous height reduction of surface islands observed in AFM. The faceted islands on the film surface tracked by AFM (Figure 2) are shown to go through full phase transition from LCO to CoO (Figure S6b,e). The LCO bulk regions are not directly probed by AFM and XPS. The yellow square in Figure 5a highlights a structural variation along the phase boundary, which is displayed in higher magnification in Figure 5b. It is shown that along the APBs LCO has completely transformed to Co_3O_4 as revealed by the rearrangement of Co atoms.[21,37] During the delithiation process, APBs can act as diffusion channels for Li^+ [30,40] but appear to have less stability and can easily convert to Co_3O_4 as a result of local atom rearrangement (Figure 5c).[21] Because of the low diffusivity of Li^+ in Co_3O_4,[21,32,40] the continued Li^+ diffusion from the LCO bulk regions to the surface regions through APBs is blocked, leaving behind unreacted regions adjacent to APBs in the bulk. This is most likely the pivotal reason for the relatively low degree of delithiation in LCO/SRO/STO(111) in comparison to LCO/SRO/STO(001) (Figure 3a) in addition to the fact that the latter has open channels for Li^+ diffusion on the surface. Previous *in situ* TEM studies on Ni-rich $LiNi_{1-x-y}Mn_xCo_yO_2$ (NMC), which has a layered *R*-3*m* phase commensurate with LCO, also showed that APBs acting as Li^+ diffusion channels can enlarge and extend across the layered structure upon delithiation.[41] A magnified view of the dotted region in Figure 5b is displayed in Figure 5d, highlighting the structure evolution from layered LCO (right) to spinel Co_3O_4 (left). The fast Fourier transform (Figure 5e) and high-resolution Co-$L_{2,3}$ edge EELS spectra (Figure 5f) collected from the two regions further support our assignment. The coexistence of Co_3O_4 and LCO phases observed by TEM is consistent with the XRD results (Figure 4a,b).

We also examined an over-delithiated LCO/SRO/STO(001) sample by STEM (Figure S7a). Cracks along the Li-containing planes are observed which appear to preferentially nucleate along the twin-boundary defects, agreeing with previous studies.[42,43] As shown in Figure S7b, more thorough phase transition is observed in LCO/SRO/STO(001) which is consistent with the relatively high degree of delithiation (Figure 3a).

CONCLUSIONS

Our results suggest that the delithiation of LCO/SRO/STO(111) involves two different pathways: Li deintercalation from {104} facets of surface islands and the continued supply of Li^+ to the surface from the film bulk via APB defect channels. During over-delithiation, surface islands can readily transform from layered LCO to rock-salt CoO, but APBs in the film bulk go through a localized phase transition to Co_3O_4 which blocks the subsequent delithiation process and prevents further loss of Li^+ from adjacent grains. In comparison, because of the presence of open channels for Li^+ diffusion, LCO/SRO/STO(001), with similar thickness, shows a relatively higher degree of delithiation. These results show that the surface topography, orientation, and defects present in cathode materials play a critical role in dictating the structural stability and electrochemical performance. Furthermore, we show that the effect of Coulombic lattice expansions on surface topography in LCO is directly dependent on the orientation of Li-containing planes, which is in turn dictated by the substrate orientation, thereby demonstrating the possibility of controlling the degree of structural deformations in LIBs by optimizing synthesis parameters. This work highlights that *in situ* AFM with nanometer scale spatial resolution on precisely synthesized model cathode materials allows for a deeper, quantitative understanding on the electrochemical degradation processes which are critical in designing robust energy storage devices.

https://doi.org/10.1021/acs.jpcc.2c01940
J. Phys. Chem. C 2022, 126, 15882−15890

■ ASSOCIATED CONTENT

Supporting Information

The Supporting Information is available free of charge at https://pubs.acs.org/doi/10.1021/acs.jpcc.2c01940.

Additional structural characterization details including XRD, 3D RSM, in-plane ϕ scans, AFM, and TEM results; Figures S1−S6 and Table S1 (PDF)
Video S1 (AVI)
Video S2 (AVI)
Video S3 (AVI)

■ AUTHOR INFORMATION

Corresponding Authors

Yingge Du − *Physical and Computational Sciences Directorate, Pacific Northwest National Laboratory, Richland, Washington 99354, United States;* orcid.org/0000-0001-9680-1950; Email: yingge.du@pnnl.gov

Jinhui Tao − *Physical and Computational Sciences Directorate, Pacific Northwest National Laboratory, Richland, Washington 99354, United States;* orcid.org/0000-0002-1156-9396; Email: jinhui.tao@pnnl.gov

Authors

Widitha Samarakoon − *Physical and Computational Sciences Directorate, Pacific Northwest National Laboratory, Richland, Washington 99354, United States; School of Chemical, Biological and Environmental Engineering, Oregon State University, Corvallis, Oregon 97331, United States*

Jiangtao Hu − *Energy and Environment Directorate, Pacific Northwest National Laboratory, Richland, Washington 99354, United States*

Miao Song − *Physical and Computational Sciences Directorate, Pacific Northwest National Laboratory, Richland, Washington 99354, United States*

Mark Bowden − *Physical and Computational Sciences Directorate, Pacific Northwest National Laboratory, Richland, Washington 99354, United States;* orcid.org/0000-0003-3812-3340

Nabajit Lahiri − *Physical and Computational Sciences Directorate, Pacific Northwest National Laboratory, Richland, Washington 99354, United States*

Jia Liu − *Energy and Environment Directorate, Pacific Northwest National Laboratory, Richland, Washington 99354, United States*

Le Wang − *Physical and Computational Sciences Directorate, Pacific Northwest National Laboratory, Richland, Washington 99354, United States;* orcid.org/0000-0002-7730-9482

Timothy Droubay − *Physical and Computational Sciences Directorate, Pacific Northwest National Laboratory, Richland, Washington 99354, United States*

Krishna Koirala − *Physical and Computational Sciences Directorate, Pacific Northwest National Laboratory, Richland, Washington 99354, United States*

Hua Zhou − *Advanced Photon Source, Argonne National Laboratory, Lemont, Illinois 60439, United States;* orcid.org/0000-0001-9642-8674

Zhenxing Feng − *School of Chemical, Biological and Environmental Engineering, Oregon State University, Corvallis, Oregon 97331, United States;* orcid.org/0000-0001-7598-5076

Complete contact information is available at: https://pubs.acs.org/10.1021/acs.jpcc.2c01940

Author Contributions

W.S. and J.H. contributed equally to this work.

Notes

The authors declare no competing financial interest.

■ ACKNOWLEDGMENTS

The work was supported by the U.S. Department of Energy (DOE), Office of Science, Office of Basic Energy Sciences (BES), Early Career Research Program, under Award 68278. XPS and X-ray diffraction studies were supported by U.S. DOE BES Materials Science and Engineering Division under Award 10122. W.S.S. acknowledges the support from PNNL-OSU Distinguished Graduate Research Fellowship. Z.F. acknowledges the support from National Science Foundation under Contracts CBET-1949870 and CBET-2016192. J.T. acknowledges the support of *in situ* AFM monitoring from U.S. DOE under Award KC020105-FWP12152. This research used resources of APS, a U.S. DOE Office of Science User Facility operated by Argonne National Laboratory under Contract DE-AC02-06CH11357. A portion of the work was performed at the W. R. Wiley Environmental Molecular Sciences Laboratory, a DOE User Facility sponsored by the Office of Biological and Environmental Research. PNNL is a multiprogram national laboratory operated for DOE by Battelle.

■ REFERENCES

(1) Mizushima, K.; Jones, P. C.; Wiseman, P. J.; Goodenough, J. B. Li_xCoO_2 (0 < x<-1): A new cathode material for batteries of high energy density. *Mater. Res. Bull.* **1980**, *15* (6), 783−789.

(2) Whittingham, M. S. Lithium Batteries and Cathode Materials. *Chem. Rev.* **2004**, *104* (10), 4271−4302.

(3) Dahéron, L.; Dedryvère, R.; Martinez, H.; Flahaut, D.; Ménétrier, M.; Delmas, C.; Gonbeau, D. Possible Explanation for the Efficiency of Al-Based Coatings on $LiCoO_2$: Surface Properties of $LiCo_{1-x}Al_xO_2$ Solid Solution. *Chem. Mater.* **2009**, *21* (23), 5607−5616.

(4) Hirayama, M.; Sonoyama, N.; Abe, T.; Minoura, M.; Ito, M.; Mori, D.; Yamada, A.; Kanno, R.; Terashima, T.; Takano, M.; et al. Characterization of electrode/electrolyte interface for lithium batteries using in situ synchrotron X-ray reflectometry—A new experimental technique for $LiCoO_2$ model electrode. *J. Power. Sources* **2007**, *168* (2), 493−500.

(5) Cheng, S.; Liu, H.; Logan, B. E. Increased performance of single-chamber microbial fuel cells using an improved cathode structure. *Electrochem. Commun.* **2006**, *8* (3), 489−494.

(6) Liu, Q.; Su, X.; Lei, D.; Qin, Y.; Wen, J.; Guo, F.; Wu, Y. A.; Rong, Y.; Kou, R.; Xiao, X.; et al. Approaching the capacity limit of lithium cobalt oxide in lithium ion batteries via lanthanum and aluminium doping. *Nat. Energy* **2018**, *3* (11), 936−943.

(7) Li, J.; Lin, C.; Weng, M.; Qiu, Y.; Chen, P.; Yang, K.; Huang, W.; Hong, Y.; Li, J.; Zhang, M.; et al. Structural origin of the high-voltage instability of lithium cobalt oxide. *Nat. Nanotechnol.* **2021**, *16* (5), 599−605.

(8) Lucero, M.; Holstun, T. M.; Yao, Y.; Faase, R.; Wang, M.; N'Diaye, A. T.; Cann, D. P.; Baio, J.; Deng, J.; Feng, Z. Dual-shell silicate and alumina coating for long lasting and high capacity lithium ion batteries. *J. Energy. Chem.* **2022**, *68*, 314−323.

(9) Jian, Z.; Wang, W.; Wang, M.; Wang, Y.; Auyeung, N.; Liu, M.; Feng, Z. Al_2O_3 coated $LiCoO_2$ as cathode for high-capacity and long-cycling Li-ion batteries. *Chin. Chem. Lett.* **2018**, *29* (12), 1768−1772.

(10) Xu, Y.; Hu, E.; Zhang, K.; Wang, X.; Borzenets, V.; Sun, Z.; Pianetta, P.; Yu, X.; Liu, Y.; Yang, X.-Q.; et al. In situ Visualization of State-of-Charge Heterogeneity within a $LiCoO_2$ Particle that Evolves

upon Cycling at Different Rates. *ACS Energy Lett.* **2017**, *2* (5), 1240−1245.
(11) See, K. A.; Wu, H.-L.; Lau, K. C.; Shin, M.; Cheng, L.; Balasubramanian, M.; Gallagher, K. G.; Curtiss, L. A.; Gewirth, A. A. Effect of Hydrofluoroether Cosolvent Addition on Li Solvation in Acetonitrile-Based Solvate Electrolytes and Its Influence on S Reduction in a Li−S Battery. *ACS Appl. Mater. Interfaces* **2016**, *8* (50), 34360−34371.
(12) Ryu, H.-H.; Namkoong, B.; Kim, J.-H.; Belharouak, I.; Yoon, C. S.; Sun, Y.-K. Capacity Fading Mechanisms in Ni-Rich Single-Crystal NCM Cathodes. *ACS Energy Lett.* **2021**, *6* (8), 2726−2734.
(13) Cabana, J.; Kwon, B. J.; Hu, L. Mechanisms of Degradation and Strategies for the Stabilization of Cathode−Electrolyte Interfaces in Li-Ion Batteries. *Acc. Chem. Res.* **2018**, *51* (2), 299−308.
(14) Zhuang, Q.; Xu, J.; Fan, X.; Wei, G.; Dong, Q.; Jiang, Y.; Huang, L.; Sun, S. $LiCoO_2$ electrode/electrolyte interface of Li-ion batteries investigated by electrochemical impedance spectroscopy. *Sci. China. B. Chem.* **2007**, *50* (6), 776−783.
(15) Laubach, S.; Laubach, S.; Schmidt, P. C.; Ensling, D.; Schmid, S.; Jaegermann, W.; Thißen, A.; Nikolowski, K.; Ehrenberg, H. Changes in the crystal and electronic structure of $LiCoO_2$ and $LiNiO_2$ upon Li intercalation and de-intercalation. *Phys. Chem. Chem. Phys.* **2009**, *11* (17), 3278−3289.
(16) Zhu, Z.; Yu, D.; Shi, Z.; Gao, R.; Xiao, X.; Waluyo, I.; Ge, M.; Dong, Y.; Xue, W.; Xu, G.; et al. Gradient-morph LiCoO2 single crystals with stabilized energy density above 3400 W h L−1. *Energy Environ. Sci.* **2020**, *13* (6), 1865−1878.
(17) Li, Z.; Yasui, S.; Takeuchi, S.; Creuziger, A.; Maruyama, S.; Herzing, A. A.; Takeuchi, I.; Bendersky, L. A. Structural study of epitaxial LiCoO2 films grown by pulsed laser deposition on single crystal $SrTiO_3$ substrates. *Thin Solid Films* **2016**, *612*, 472.
(18) Yang, Z.; Ong, P. V.; He, Y.; Wang, L.; Bowden, M. E.; Xu, W.; Droubay, T. C.; Wang, C.; Sushko, P. V.; Du, Y. Direct Visualization of Li Dendrite Effect on $LiCoO_2$ Cathode by In Situ TEM. *Small* **2018**, *14* (52), e1803108.
(19) Qin, C.; Wang, L.; Yan, P.; Du, Y.; Sui, M. LiCoO2 Epitaxial Film Enabling Precise Analysis of Interfacial Degradations. *Chin. Phys.* **2021**, *38* (6).
(20) Nishio, K.; Ohnishi, T.; Akatsuka, K.; Takada, K. Crystal orientation of epitaxial $LiCoO_2$ films grown on SrTiO 3 substrates. *J. Power Sources* **2014**, *247*, 687−691.
(21) Tan, H.; Takeuchi, S.; Bharathi, K. K.; Takeuchi, I.; Bendersky, L. A. Microscopy Study of Structural Evolution in Epitaxial $LiCoO_2$ Positive Electrode Films during Electrochemical Cycling. *ACS Appl. Mater. Interfaces* **2016**, *8* (10), 6727−35.
(22) Takeuchi, S.; Tan, H.; Bharathi, K. K.; Stafford, G. R.; Shin, J.; Yasui, S.; Takeuchi, I.; Bendersky, L. A. Epitaxial $LiCoO_2$ films as a model system for fundamental electrochemical studies of positive electrodes. *ACS Appl. Mater. Interfaces* **2015**, *7* (15), 7901−11.
(23) Ohnishi, T.; Takada, K. Epitaxial Thin-Film Growth of SrRuO3, Sr3Ru2O7, and $Sr2RuO_4$ from a $SrRuO_3$ Target by Pulsed Laser Deposition. *Appl. Phys. Express* **2011**, *4* (2), 025501.
(24) Doh, C. H.; Kim, D. H.; Kim, H. S.; Shin, H. M.; Jeong, Y. D.; Moon, S. I.; Jin, B. S.; Eom, S. W.; Kim, H. S.; Kim, K. W.; et al. Thermal and electrochemical behaviour of C/Li_xCoO2 cell during safety test. *J. Power Sources* **2008**, *175* (2), 881−885.
(25) Hu, J.; Li, L.; Hu, E.; Chae, S.; Jia, H.; Liu, T.; Wu, B.; Bi, Y.; Amine, K.; Wang, C.; et al. Mesoscale-architecture-based crack evolution dictating cycling stability of advanced lithium ion batteries. *Nano Energy* **2021**, *79*, 105420.
(26) Bi, Y.; Tao, J.; Wu, Y.; Li, L.; Xu, Y.; Hu, E.; Wu, B.; Hu, J.; Wang, C.; Zhang, J.-G.; et al. Reversible planar gliding and microcracking in a single-crystalline Ni-rich cathode. *Science* **2020**, *370* (6522), 1313−1317.
(27) Motohashi, T.; Katsumata, Y.; Ono, T.; Kanno, R.; Karppinen, M.; Yamauchi, H. Synthesis and Properties of CoO_2, the $x = 0$ End Member of the Li_xCoO_2 and Na_xCoO_2 Systems. *Chem. Mater.* **2007**, *19* (21), 5063−5066.
(28) Lu, D.; Tao, J.; Yan, P.; Henderson, W. A.; Li, Q.; Shao, Y.; Helm, M. L.; Borodin, O.; Graff, G. L.; Polzin, B.; et al. Formation of Reversible Solid Electrolyte Interface on Graphite Surface from Concentrated Electrolytes. *Nano Lett.* **2017**, *17* (3), 1602−1609.
(29) Tao, J.; Battle, K. C.; Pan, H.; Salter, E. A.; Chien, Y.-C.; Wierzbicki, A.; De Yoreo, J. J. Energetic basis for the molecular-scale organization of bone. *Proc. Natl. Acad. Sci. U. S. A.* **2015**, *112* (2), 326−331.
(30) Ong, P.-V.; Yang, Z.; Sushko, P. V.; Du, Y. Formation, Structural Variety, and Impact of Antiphase Boundaries on Li Diffusion in $LiCoO_2$ Thin-Film Cathodes. *J. Phys. Chem. Lett.* **2018**, *9* (18), 5515−5520.
(31) Kramer, D.; Ceder, G. Tailoring the Morphology of $LiCoO_2$: A First Principles Study. *Chem. Mater.* **2009**, *21* (16), 3799−3809.
(32) Hasegawa, G.; Kuwata, N.; Tanaka, Y.; Miyazaki, T.; Ishigaki, N.; Takada, K.; Kawamura, J. Tracer diffusion coefficients of Li^+ ions in c-axis oriented Li_xCoO_2 thin films measured by secondary ion mass spectrometry. *Phys. Chem. Chem. Phys.* **2021**, *23* (3), 2438−2448.
(33) Zheng, X.; Huang, T.; Fang, G.; Pan, Y.; Li, Q.; Wu, M. Di(methylsulfonyl) Ethane: New Electrolyte Additive for Enhancing $LiCoO_2$/Electrolyte Interface Stability under High Voltage. *ACS Appl. Mater. Interfaces* **2019**, *11* (39), 36244−36251.
(34) Lu, W.; Zhang, J.; Xu, J.; Wu, X.; Chen, L. In Situ Visualized Cathode Electrolyte Interphase on $LiCoO_2$ in High Voltage Cycling. *ACS Appl. Mater. Interfaces* **2017**, *9* (22), 19313−19318.
(35) Ohzuku, T.; Ueda, A. Solid-State Redox Reactions of $LiCoO_2$ (R3m) for 4 V Secondary Lithium Cells. *J. Electrochem. Soc.* **1994**, *141* (11), 2972−2977.
(36) Reimers, J. N.; Dahn, J. R. Electrochemical and In Situ X-Ray Diffraction Studies of Lithium Intercalation in Li_xCoO_2. *J. Electrochem. Soc.* **1992**, *139* (8), 2091−2097.
(37) Qin, C.; Jiang, Y.; Yan, P.; Sui, M. Revealing the minor Li-ion blocking effect of $LiCoO_2$ surface phase transition layer. *J. Power Sources* **2020**, *460*, 228126.
(38) Li, N.; Sun, M.; Kan, W. H.; Zhuo, Z.; Hwang, S.; Renfrew, S. E.; Avdeev, M.; Huq, A.; McCloskey, B. D.; Su, D.; et al. Layered-rocksalt intergrown cathode for high-capacity zero-strain battery operation. *Nat. Commun.* **2021**, *12* (1)..
(39) Biesinger, M. C.; Payne, B. P.; Grosvenor, A. P.; Lau, L. W. M.; Gerson, A. R.; Smart, R. S. C. Resolving surface chemical states in XPS analysis of first row transition metals, oxides and hydroxides: Cr, Mn, Fe, Co and Ni. *Appl. Surf. Sci.* **2011**, *257* (7), 2717−2730.
(40) Balke, N.; Jesse, S.; Morozovska, A. N.; Eliseev, E.; Chung, D. W.; Kim, Y.; Adamczyk, L.; Garcia, R. E.; Dudney, N.; Kalinin, S. V. Nanoscale mapping of ion diffusion in a lithium-ion battery cathode. *Nat. Nanotechnol.* **2010**, *5* (10), 749−54.
(41) Li, S.; Yao, Z.; Zheng, J.; Fu, M.; Cen, J.; Hwang, S.; Jin, H.; Orlov, A.; Gu, L.; Wang, S.; et al. Direct Observation of Defect-Aided Structural Evolution in a Nickel-Rich Layered Cathode. *Angew. Chem.* **2020**, *132* (49), 22276−22283.
(42) Blochwitz, C.; Tirschler, W. Twin boundaries as crack nucleation sites. *Cryst. Res. Technol.* **2005**, *40* (1−2), 32−41.
(43) Grilli, N.; Cocks, A. C. F.; Tarleton, E. Modelling the nucleation and propagation of cracks at twin boundaries. *Int. J. Fract.* **2022**, *233*, 17−38.

https://doi.org/10.1021/acs.jpcc.2c01940
J. Phys. Chem. C 2022, 126, 15882−15890